Extracting spacing-derived estimates of rod density in healthy retinae

HEATHER HEITKOTTER,[1,8] ⓘ EMILY J. PATTERSON,[2,8] ⓘ ERICA N. WOERTZ,[3] JENNA A. CAVA,[4] MINA GAFFNEY,[5] INIYA ADHAN,[6] JOHNNY TAM,[7] ⓘ ROBERT F. COOPER,[4,5] ⓘ AND JOSEPH CARROLL[1,4,5,*] ⓘ

[1]*Department of Cell Biology, Neurobiology and Anatomy, Medical College of Wisconsin, Milwaukee, WI, USA*
[2]*UCL Institute of Ophthalmology, University College London, London, UK*
[3]*John A. Moran Eye Center, University of Utah, Salt Lake City, UT, USA*
[4]*Department of Ophthalmology and Visual Sciences, Medical College of Wisconsin, Milwaukee, WI, USA*
[5]*Joint Department of Biomedical Engineering, Marquette University and Medical College of Wisconsin, Milwaukee, WI, USA*
[6]*School of Medicine, Medical College of Wisconsin, Milwaukee, WI, USA*
[7]*National Eye Institute, National Institutes of Health, Bethesda, MD, USA*
[8]*These authors contributed equally to this work*
[*]jcarroll@mcw.edu

Abstract: Quantification of the rod photoreceptor mosaic using adaptive optics scanning light ophthalmoscopy (AOSLO) remains challenging. Here we demonstrate a method for deriving estimates of rod density and rod:cone ratio based on measures of rod spacing, cone numerosity, and cone inner segment area. Twenty-two AOSLO images with complete rod visualization were used to validate this spacing-derived method for estimating density. The method was then used to estimate rod metrics in an additional 105 images without complete rod visualization. The spacing-derived rod mosaic metrics were comparable to published data from histology. This method could be leveraged to develop large normative databases of rod mosaic metrics, though limitations persist with intergrader variability in assessing cone area and numerosity.

1. Introduction

Adaptive optics scanning light ophthalmoscopy (AOSLO) enables noninvasive, high-resolution, *in vivo* characterization of the cone mosaic, both in healthy eyes and those with retinal pathology [1]. Cones are relatively easily imaged using confocal (to visualize cone outer segments) and split detection (to visualize cone inner segments) modalities [2,3]. With these tools, it is possible to derive various quantitative metrics of the cone mosaic directly from AOSLO images (e.g., cone density, spacing, and regularity) [4,5]. There have been dozens of studies characterizing cone metrics in a range of retinal diseases [1], and at multiple eccentricities [6,7]. Central to the clinical advancement of these metrics as biomarkers is having robust normative data [7–11], as well as detailed information on the sensitivity of various metrics [4]. While the cone mosaic has been extensively analyzed with AOSLO, fewer studies have focused on the rod mosaic. Rods play a significant role in retinal and neurological pathologies [12–14], are vulnerable to degeneration with age [15–18], and are suggested as a therapeutic target in many forms of blindness [19]. Challenges associated with imaging the complete rod mosaic have hindered widespread *in vivo* quantitative analysis of rod structure in normal and diseased eyes. Most of the information available related to rod structure and topography has been completed through post-mortem histology [20,21], which is inadequate for creating large normative databases that are critical for the development and validation of rod biomarkers for monitoring disease progression and

therapeutic response. As such, there is a need to establish accurate normative measurements of the rod mosaic *in vivo*.

One of the first accounts of *in vivo* visualization of the healthy rod mosaic was completed using an AO flood-illuminated system where multiple images were collected with visible and near-infrared light sources (650 and 750 nm) at the same retinal location following a 10 second exposure to a 550 nm light to bleach the retina [22]. Images were filtered to reduce diffraction blur and deconvolved for enhanced image contrast prior to image registration and summation. This provided partial visualization of the rod mosaic, which enabled derivation of rod and cone modal spacing at each location [22]. More recently, AOSLO has been used to visualize the rod mosaic in healthy and diseased retinae and determine rod spacing using the density recovery profile [23], although direct rod counts were not feasible and rod spacing estimates in healthy eyes were higher than expected based on prior histological studies. Rod visualization with AOSLO is enhanced through the use of high speed imaging to mitigate image artifacts due to retinal motion [24], averaging images over time [25,26], averaging images collected at varying depths of focus [11], or use of a sub-Airy disc confocal pinhole (with or without an annular pupil illumination mask) [25,27]. With an increased understanding of how to obtain high-resolution images of the rod mosaic, it has been possible to quantify structural metrics across various retinal locations in healthy eyes, including estimates of rod and cone density, as well as the rod:cone ratio, that are comparable to histological studies [11,25]. AO systems that integrate both SLO and optical coherence tomography may facilitate deeper characterization of the rod mosaic in healthy and diseased retinae, although no quantitative metrics have been published [28].

Although rods outnumber cones by a 20:1 ratio in the human retina [20], several factors limit reliable visualization of rods, including rod cell size being close to the resolution limit of confocal AOSLO (for which the system must be optimized) [2,25], the reduced waveguiding capacity of rods compared to cones [29,30], differences in depth of focus required to adequately resolve rods versus cones [25], and the fact that the rod mosaic is interspersed with cones, thereby reducing its regularity [31]. Although standard split detection AOSLO enables disambiguation of cones within a given region of interest (ROI), it most often cannot resolve rod or foveal cone inner segments in a healthy retina [3]. These factors contribute to ongoing challenges associated with accurate visualization and quantification of healthy rods. Previous work evaluating the sensitivity of various structural cone metrics demonstrated that nearest neighbor distance (NND) is highly insensitive to cells missed in the counting process [4]. This suggests that ROIs with incompletely resolved mosaics can be used to produce a reliable NND estimate, as long as some cells can be resolved. The purpose of this study was to demonstrate a method for producing spacing-derived estimates of rod density in individuals with contiguous photoreceptor mosaics, using measures of rod spacing and estimates of cone area within a given ROI. We demonstrate that this spacing-derived method yields estimates of rod density that are comparable to those obtained using direct counts in mosaics for which every rod can be visualized. We then obtained spacing-derived estimates in additional healthy participants and retinal locations to begin to establish a normative dataset of rod density and rod:cone ratio.

2. Methods

This study followed the tenets of the Declaration of Helsinki and was approved by the Institutional Review Board at the Medical College of Wisconsin (PRO17439). Written informed consent was obtained from all participants after explanation of the nature and possible risks associated with this imaging study.

A total of 24 eyes in 21 participants (collected between July 2014 – July 2022; 13 females, 8 males; age range: 20-61 years) were analyzed for this study (for demographics, Table 1). Axial length and corneal curvature were measured prior to dilation using a Zeiss IOL Master 500 (Carl Zeiss Meditec, Dublin, CA, USA). Refractive error was estimated using a Topcon KR-800S Auto

Kerato-Refractometer (Topcon Medical Systems, Inc., Oakland, NJ, USA). Ocular biometry measures of axial length (mm), corneal curvature (diopters, D), and spherical refractive error (D) for each eye included in this study are provided in Table 1. The eye to be imaged was subsequently dilated. Cycloplegia or mydriasis was induced with administration of one drop each of 2.5% phenylephrine hydrochloride (Akorn, Lake Forest, IL, USA) and 1% tropicamide (Akorn, Lake Forest, IL, USA) or (in participants with a history of incomplete cycloplegia using phenylephrine hydrochloride and tropicamide) one drop of 1% Cyclomydril (cyclopentolate hydrochloride, phenylephrine hydrochloride; Alcon Laboratories, Inc. Fort Worth, Texas, USA).

2.1. AOSLO imaging and processing

A previously described AOSLO system (see [2,3]) was used to image retinal locations extending from the center of fixation up to approximately 20° eccentricity (when possible) along the temporal meridian in 1° increments. Confocal and non-confocal (split detection) images were obtained simultaneously at each imaging location. The participant's pupil was aligned and stabilized with the use of a dental impression on a bite bar mounted to a three-axis translation stage. Either an external light source or digital light projector-based internal fixation target was used to guide the participant's fixation [33]. The eye's wavefront was detected over an 8 mm diameter pupil using an 850 nm superluminescent diode (SLD; Superlum, Carrigtwohill, Co., Cork, Ireland) and a custom Shack-Hartman sensor [2], and the wavefront was corrected by a Hi-speed DM97 deformable mirror (ALPAO S.A.S., Biviers, Grenoble, France). The confocal imaging channel was equipped with a confocal aperture that ranged between 0.8–1.2 Airy disc diameters. AOSLO imaging sequences consisting of 150 frames each were collected using either a 775 nm or 790 nm SLD (Superlum, Carrigtwohill, Co., Cork, Ireland) over a field size of 1.0° x 1.0° and 1.5° x 1.5°. In most cases, multiple imaging sequences were recorded at the same location either over time or using a through-focus technique (0.1D steps ranging 1D in depth of focus) to facilitate rod visualization.

For each image sequence, intra-frame distortion from the resonant scanner was corrected [34], a reference frame for each imaging sequence was selected [35], to which the other frames were registered and averaged [34], and residual distortion due to eye motion in the processed image was estimated and corrected [36,37]. Processed confocal and split detection images for each participant were aligned and montaged simultaneously using custom software [37], which outputs to Adobe Photoshop CS6 (Adobe Systems, San Jose, CA, USA). The linear scale (µm/pixel) of AOSLO data for each participant was estimated based on individual ocular biometry measures as previously described [38], using the equation below:

$$\text{AOSLO Scale} = \frac{\text{T}}{\text{f}_1 \text{T}_\text{s}} \left(\frac{180}{\pi} \right) \text{RMF} \left(\frac{\text{AL}}{24} \right)$$

Where T represents the periodicity of a Ronchi ruling (µm/cycle), f_1 represents the focal length of the model eye in our system (µm), T_s represents the sampling period of the lines in the model eye image of the Ronchi ruling (pixels/cycle), RMF represents the assumed retinal magnification factor (291 µm/degree) of an eye with a 24.0 mm axial length [39], and AL is the participant's axial length (mm).

While adequate rod visualization was possible in individual images at some retinal locations for some participants, additional processing was required at locations where multiple imaging sequences were collected at multiple time points or multiple levels of focus. These images were input to a separate Photoshop file and aligned and cropped to common area. Images with poor visualization of rods were excluded. These cropped images were then exported from Photoshop and compiled to create separate confocal and split detection videos (.AVIs) using ImageJ [40]. The ImageJ-created videos were then registered and averaged as described above to produce a final image for a given location [34,36]. The resultant image was then added to the original

Table 1. Participant demographics and retinal locations used for rod metrics

Participant ID	Sex (M/F)	Eye (OD/OS)	AL (mm)	Corneal Curvature (K1/K2; D)	Spherical Refractive Error (D)	ROI's Used for Rod Analyses Total (Direct)	ROI Locations (Degrees)[b]
JC_0200	M	OS	24.67	43.27/43.89	-3.00	4 (0)	8.7, 9.5, 10.2, 11.4
JC_0677	F	OS	24.01	42.03/42.94	-1.25	2 (2)	**9.1, 10.0**
JC_10220	F	OD	22.92	43.05/43.44	+0.75	12 (0)	9.9, 10.4, 11.0, 11.9, 13.9, 14.8, 16.2, 17.1, 18.5, 19.7, 20.1, 21.5
JC_10549	M	OD	23.98	44.29/45.12	-1.75	3 (0)	6.9, 8.0, 10.8
JC_10549	M	OS	23.99	44.88/45.36	-1.50	7 (0)	10.1, 10.5, 11.6, 12.6, 13.7, 14.9, 16.3
JC_10567	F	OD	22.32	45.06/45.42	+0.50	15 (3)	**5.2, 6.3, 7.6,** 7.8, 8.8, 8.9, 9.2, 9.8, 9.81, 10.4, 10.5, 10.6, 11.2, 12.6, 14.6
JC_10567[a]	F	OS	22.40	45.06/45.42	-0.50	NA	NA
JC_10586	F	OD	21.37	45.12/46.75	+3.50	9 (0)	3.9, 4.8, 5.8, 6.7, 7.4, 8.6, 9.7, 10.5, 11.0
JC_11441[a]	F	OD	23.13	44.58/45.49	-1.75	3 (0)	5.3, 7.3, 9.0
JC_11442	M	OD	23.70	43.1/43.21	-0.25	3 (0)	5.9, 7.0, 10.3
JC_11442[a]	M	OS	23.63	43.05/43.55	+0.00	NA	NA
JC_11591[a]	M	OD	24.44	41.77/44.00	-2.75	NA	NA
JC_11658	F	OS	22.29	44.58/45.36	-1.00	5 (0)	6.1, 7.3, 8.6, 9.8, 10.8
JC_11660[a]	F	OD	23.14	42.13/42.29	+2.00	13 (3)	**5.5, 6.3, 9.4,** 9.7, 10.1, 10.3, 11.6, 12.1, 12.8, 13.7, 14.5, 15.1, 15.7
JC_11686	F	OD	23.51	42.99/44.23	-1.25	2 (2)	**7.2, 10.5**
JC_12019	F	OS	23.84	41.72/44.00	-0.75	11 (0)	8.6, 9.5, 11.3, 13.6, 14.1, 15.4, 16.2, 16.4, 17.0, 17.6, 18.1
JC_12255	M	OD	23.73	42.35/43.66	-0.50	4 (0)	6.0, 7.3, 7.9, 9.0
JC_12276	F	OD	22.51	44.70/45.12	+0.25	8 (8)	**2.2, 3.0, 4.0, 6.8, 7.9, 8.8, 9.8, 11.6**
JC_12294	M	OD	24.86	42.99/43.49	-0.50	1 (0)	7.9
JC_12351	F	OD	24.58	42.35/43.21	-0.75	5 (0)	7.9, 9.1, 9.8, 10.8, 10.81
JC_12358	M	OD	23.26	44.58/45.18	-0.75	2 (0)	9.9, 10.9
JC_12421	F	OS	21.61	45.18/45.55	+0.75	2 (0)	9.4, 10.3
JC_12422	M	OS	24.08	40.76/41.01	+2.50	6 (4)	**4.3, 5.3, 6.4,** 8.1, 10.0, **10.8**
JC_12479	F	OD	23.00	44.53/44.70	-1.00	10 (0)	3.3, 6.3, 6.9, 8.0, 8.9, 9.6, 10.6, 11.5, 12.7, 13.7

[a]Denotes eyes used for foveal cone analysis; data was previously published by Cava et al. [32]
[b] Bold values indicate ROI locations used for direct versus spacing-derived validation study (n = 22)

montage. All montages were imported into Mosaic Analytics (v0.6.8.9, Translational Imaging Innovations, Inc., Hickory NC) to extract 100×100 μm confocal and split detection ROIs for subsequent quantification of the photoreceptor mosaic. The location of each ROI was calculated based on retinal distance, in μm, from the estimated position of peak cone density in each montage.

2.2. Cone identification

Cones in split-detection ROIs were semi-automatically identified using Mosaic Analytics, including those that were not completely within the confines of the ROI (termed "edge cones"). These cone coordinates were used to determine the number of bound and un-bound cones, and the total bound cone area using custom software (Metricks Master v0.1.5.2; https://github.com/Eurybiadan/Metricks) [4]. A cone is defined as "bound" if the vertices of its Voronoi domain are all contained within the ROI.

2.3. Estimating cone area

The area of *individual* cones within the split detection ROIs was derived using custom semi-automatic segmentation software (see Fig. 1) [41]. The initial input parameters for segmentation were set at 100 for the Hessian response and at 2 for the geodesic active contour iteration number. From this automatically generated segmentation, cells were removed from the analysis when the segmented outline encompassed edge cones or was otherwise inaccurate. Segmentations that under- or over-estimated the area occupied by a cone were manually corrected (Fig. 1). Manually segmented cones were also added when high contrast cones without automatic segmentation were present. Within each ROI, a minimum of 30 segmentations were used to estimate the average area of an individual cone for that ROI.
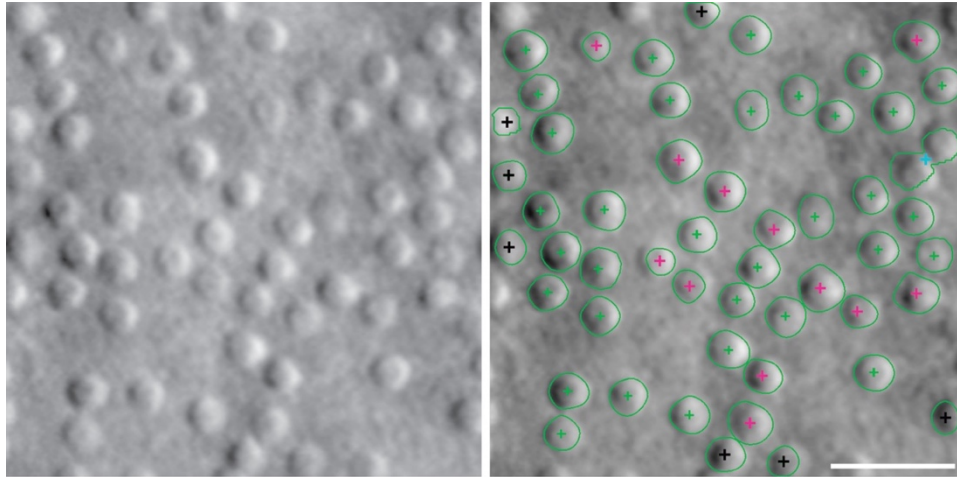

Fig. 1. Split-detection ROI (left) at ~T10 (JC_10220) with corresponding uncorrected cone segmentation output (right). The boundary of each cell produced by the segmentation software is shown as a thin green line with the center of the cell denoted with a + sign. Inaccurate cell segmentations whereby two cells were segmented together (denoted with blue + sign) and segmentations of cones near the edges of the ROI (denoted with black + signs) were removed. Segmentations that were deemed to under- or over-estimate the cone boundary (pink + signs) were manually corrected prior to estimating cone area. Scale bar = 25 μm.

2.4.   Estimating modal spacing of the rod mosaic – intercell distance

To produce a method for spacing-derived rod density estimation we require an estimate of the modal rod spacing, which for a contiguous mosaic of a single cell type (*e.g.*, foveal cone mosaic) would be equal to the average intercell distance (ICD). However, the ICD of the rod mosaic will overestimate the modal spacing of neighboring rods due to the presence of cones in the mosaic. In contrast, NND is known to be a highly robust cell spacing metric that is unaffected by cells missed during the cell identification process or discontinuities in the mosaic. We thus determined the relationship between bound NND and bound ICD for a contiguous cone mosaic. Using previously acquired confocal AOSLO data [32], we extracted 50 ROIs (each 30×30 µm) from five individuals with contiguous foveal cone mosaics (5 eyes; 3 females, 2 males; 23-27 years; Table 1). Cone NND and ICD were calculated using custom software (Metricks Master v0.1.5.2) [4]. These data demonstrated a strong linear relationship between bound NND and bound ICD, where ICD = 1.1298(NND) + 0.1487 (Fig. 2).
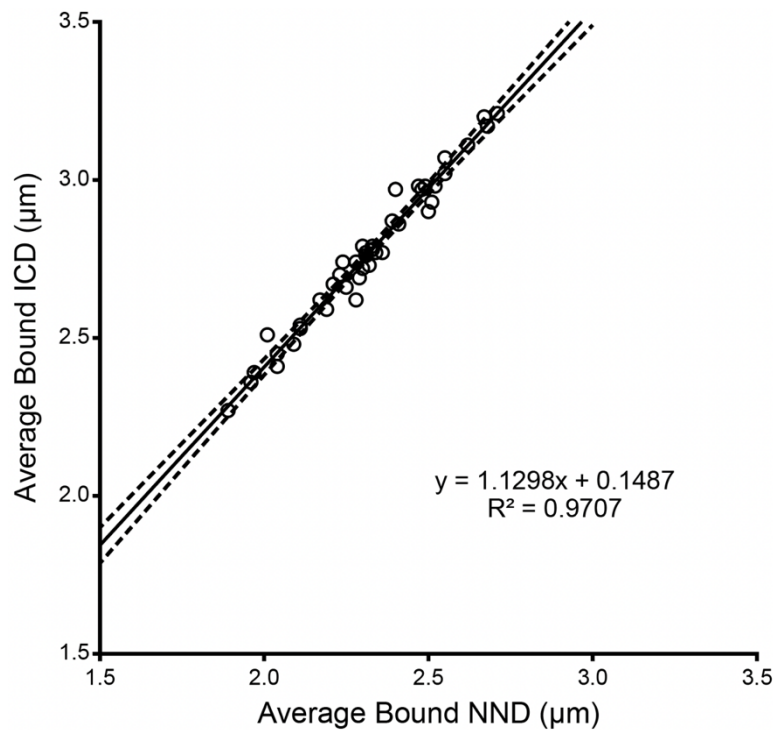

Fig. 2. A strong linear relationship is found between average bound intercell distance (ICD) and average bound nearest neighbor distance (NND) for cone photoreceptors within a contiguous mosaic. A solid black line denotes the linear regression for the data shown with dashed black lines representing the 95% confidence intervals for the regression. A total of 50 foveal ROIs were measured (open circles). While by definition NND is always lower than ICD, there was a strong linear correlation between bound ICD and bound NND, which enabled estimation of bound ICD from bound NND for a contiguous mosaic.

Prior to analyzing rods in the confocal ROIs, cone coordinates produced from section 2.2 were overlaid onto the corresponding confocal ROI, and the size of each coordinate inflated (diameter range 5-7 pixels), so the cones within the confocal ROI were "masked" for rod analysis. Following "masking" of the cones, rods in confocal ROIs were counted manually using Mosaic Analytics, and rod NND was calculated using custom software (Metricks Master v0.1.5.2) [4].

We then estimated bound rod ICD derived from the bound rod NND for each ROI, using the theoretical relationship between ICD & NND derived from the contiguous foveal cone mosaics as shown in Fig. 2.

2.5. Estimating spacing-derived rod density

To produce an estimate of rod density, we converted bound rod ICD spacing values from retinal distance in μm to an angular measure (modal spacing; cycles/degree) as previously described [42,43]. It is important to note that this conversion relies on the assumption of a triangularly-packed mosaic. However, rod density derived only from rod spacing overestimates the number of cells in a given retinal area, as it assumes a complete, contiguous mosaic. Therefore, we utilized the number of bound cones and average cone area to calculate the percentage of retinal area occupied by cones for each ROI. We then adjusted the spacing-derived rod density estimate to account for the presence of cones.

2.6. Comparison of cone-corrected spacing-derived rod density estimates to direct rod count density

From our study population, a total of 22 ROIs between 2.2-11.6° temporal to the fovea from six participants (6 eyes from 6 participants; 5 females, 1 male; age range: 20-58 years) with complete visualization of the rod mosaic were chosen for the validation study (Table 1, bold ROI locations). These high quality images allowed a single grader (HH) to determine a direct, bound rod density estimate and bound rod NND using custom software (Metricks Master v0.1.5.2) [4]. Spacing-derived rod density was validated against direct estimates of bound rod density from these 22 ROIs using Bland-Altman analysis [44–46]. After verifying that there was minimal bias between the two methods of estimating rod density, spacing-derived rod density was calculated for a larger normative dataset.

2.7. Establishing normative data for spacing-derived rod density and rod:cone ratio

An additional 105 ROIs ranging from 3.3-21.5° temporal to the fovea from 18 eyes of 17 participants included in this study were then analyzed (Table 1). Most of these ROIs did not have complete visualization of the rod mosaic, but clusters of rods were visible and countable. One grader (HH) repeated the same protocol described above to evaluate the cone and rod mosaics of these ROIs – the only difference being that no direct density estimates were available for comparison. For each ROI, rod:cone ratio was determined by taking the ratio of the spacing-derived rod density estimate and the bound cone density estimate. For these 105 ROIs and the 22 used for the method validation (127 total from 21 eyes), spacing-derived rod mosaic metrics were compared with previous histological [20] and AOSLO estimates of rod density and rod:cone ratio [11].

2.8. Evaluation of repeatability and reliability of spacing-derived rod density

As mentioned above, the spacing-derived estimate of rod density described here assumes a complete, contiguous mosaic, which must account for the area occupied by cones. As NND is a highly robust spacing metric, the cone metrics (i.e., individual cone area and the number of cones identified in an ROI) represent the largest potential sources of error in the final spacing-derived estimate of rod density. To assess these sources of error, three additional graders (EJP, ENW, IA) completed cone counts and segmentations twice for the 22 ROIs where direct rod counts were available for comparison. In addition, the original grader (HH) completed a second set of cone counts and segmentations for these ROIs.

The repeatability and reliability of spacing-derived rod density estimates were evaluated using intragrader standard deviation, Sw, to calculate the repeatability coefficient (2.77 x Sw) and measurement error (1.96 x Sw) [47]. Rod density estimates for each grader were evaluated for

intragrader repeatability using the intraclass correlation (R Studio v1.4.1103). The two sets of data from each grader were then averaged and intergrader reliability was assessed using one-way analysis of variance (ANOVA) with GraphPad Prism (v9.0.0) for Windows (La Jolla, CA, USA). Unless otherwise mentioned, calculations were completed in either GraphPad Prism or Microsoft Excel.

3. Results

Representative ROIs with complete visualization of the rod mosaic that were used for the spacing-derived rod density method validation are shown in Fig. 3. Bland-Altman analysis of one grader's (HH) rod density from direct counts and spacing-derived estimates demonstrated a mean bias of 0.14%, or 395 rods/mm^2, with the limits of agreement between -30.5% and 30.7%, or -24,723 (95% CI: -33,764 to -15,682 rods/mm^2) and 25,514 rods/mm^2 (95% CI: 16,473 to 34,555 rods/mm^2; Fig. 4). With evidence to suggest that spacing-derived estimates of rod density are on average comparable to direct count estimates, we sought to expand our normative dataset to include ROIs where only some of the rod mosaic was visualizable, although all of the cones in the mosaic were visible. These ROIs ranged in retinal eccentricity between 3.9 and 21.5° temporal to the fovea, with some of these retinal locations shown in Fig. 5. The spacing-derived estimates of rod density from these ROIs, in addition to the spacing-derived estimates from the 22 ROIs with complete rod mosaic visualization, were plotted as a function of retinal eccentricity as open circles (Fig. 6(A)). Direct count rod density for the 22 ROIs with complete rod visualization were included as filled black circles on this graph, for a total of 139 data points (Fig. 6(A)). These data fall between published histological [20] and AO-derived [11] estimates of rod density. Our estimates of rod:cone ratio were also plotted as a function of retinal eccentricity along with previous histological [20] and AO-derived [11] estimates (Fig. 6(B)). Rod:cone ratio estimates in the 22 ROIs with complete rod visualization were calculated from both spacing-derived (open circles) and direct count (filled black circles) rod density measures and plotted together, totaling 149 data points.
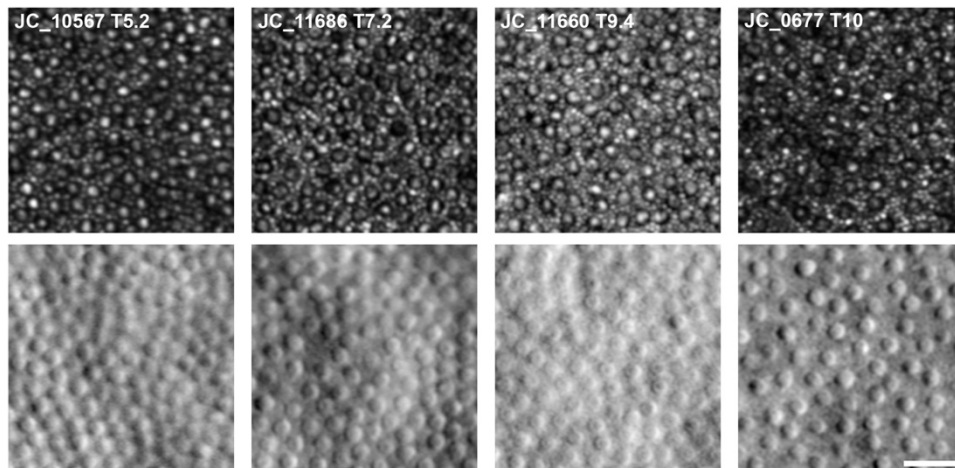

Fig. 3. Representative ROIs with complete rod mosaic visualization. ROIs (top, confocal; bottom, split detection) between T5 and T10 from four participants with complete visualization of the rod mosaic in a 100×100 μm area are displayed. All ROIs have been resized to a common scale for display purposes. Scale bar = 25 μm. See Dataset 1, Ref. [48] to access all ROIs, and associated coordinate files, with complete visualization of the rod mosaic.
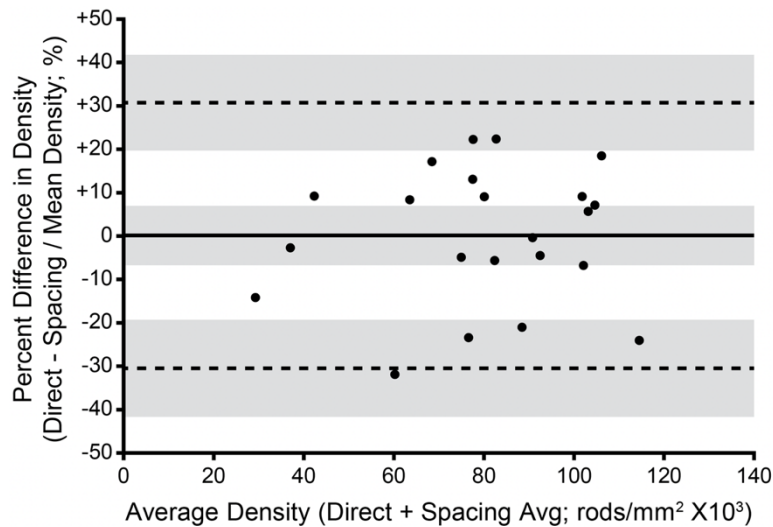
Fig. 4. Bland-Altman plot comparing spacing-derived rod density to direct estimates of rod density for the 22 ROIs in which all rods were visible. The mean difference between density estimation methods was 0.14% (95% CI: -6.8 to 7.1%), with limits of agreement of 30.7% (95% CI: 19.7 to 41.8%) and -30.5% (95% CI: -19.4 to -41.5%). The solid black line represents the average percent difference in rod density between methods; dashed lines represent the 95% limits of agreement; gray shading represents the 95% confidence intervals. See Data File 1 for underlying values.

We evaluated the repeatability of cone-corrected rod density, derived from spacing, for the four graders that counted and segmented cones twice in these ROIs (Table 2). Overall, graders produced spacing-derived rod density estimates that were fairly repeatable, with repeatability coefficients ranging from 9,995–25,005 rods/mm^2 (12.5–32.7%). Intragrader repeatability was good for all graders in this study (ICC = 0.861–0.978). However, it is important to note that data quality (i.e., the level of contrast within split-detection images) and grader experience with cone segmentation likely contributes to the variance observed across repeated measures.

Intergrader reliability was evaluated by comparing the mean spacing-derived rod density produced by each of the four graders for each ROI. These values passed the normality test for every grader (p = 0.42–0.82, Shapiro-Wilk), so a one-way ANOVA was performed to compare rod density estimates across graders. This analysis revealed a statistically significant difference in rod density estimates between at least two graders (F(1.67, 35.1) = 5.99, p = 0.0085). Tukey's multiple comparisons test revealed that mean rod density was significantly different between graders 1 and 2 (p = 0.016, 95% CI = 956 to 11,127 rods/mm^2) as well as graders 1 and 3 (p < 0.0001, 95% CI = 4,204 to 9,853 rods/mm^2). No statistically significant difference in mean rod density was observed between graders 1 and 4 (p = 0.14), graders 2 and 3 (p = 0.90), graders 2 and 4 (p = 0.76), or graders 3 and 4 (p = 0.29).
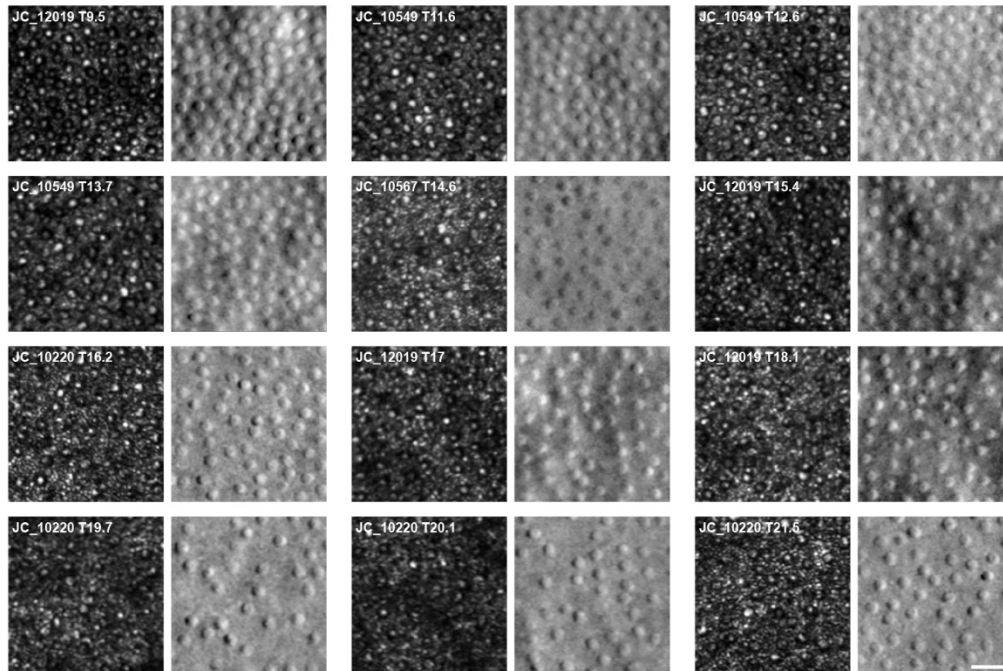
Fig. 5. Example ROIs where spacing-derived rod density was estimated with incomplete visualization of the rod mosaic. ROIs (left, confocal; right, split detection) from four participants with some degree of visualization of the rod mosaic in retinal locations between approximately T10 and T21. All ROIs have been resized to a common scale. Scale bar = 25 μm. See Dataset 2, Ref. [49] for access to all ROI and corresponding coordinate files used for spacing-derived rod density estimates.

Table 2. Repeatability of spacing-derived rod density measurements

Metric[a]	Grader 1	Grader 2	Grader 3	Grader 4
Measurement Error (95% CI), rods/mm^2	7,072	9,217	9,745	17,693
	(6,006–8,139)	(7,827–10,606)	(8,276–11,215)	(15,026–20,360)
Measurement Error (95% CI), %	8.9	12.5	13.4	23.1
	(7.5–10.2)	(10.6–14.4)	(11.4–15.4)	(19.7–26.7)
Repeatability Coefficient (95% CI), rods/mm^2	9,995	13,026	13,773	25,005
	(8,929–11,061)	(11,636–14,415)	(12,304–15,242)	(22,338–27,673)
Repeatability (95% CI), %	12.5	17.7	18.9	32.7
	(11.2–13.9)	(15.8–19.5)	(16.9–20.9)	(29.2–36.2)
ICC (95% CI)	0.978	0.974	0.960	0.861
	(0.959–0.996)	(0.952–0.996)	(0.927–0.993)	(0.752–0.970)

[a]*Measurement error and repeatability were calculated using within participant standard deviation, *Sw*, as described by Bland and Altman (1996) [47]. Measurement error is 1.96x*Sw*, with the difference between a measurement and the true value expected to fall below this value for 95% of observations. The repeatability coefficient is 2.77x *Sw*, with the difference between two measurements by a given grader for the same image expected to fall below this value for 95% of paired observations. See Data File 1 and Dataset 1 [48], for underlying values and corresponding ROIs with coordinate files.
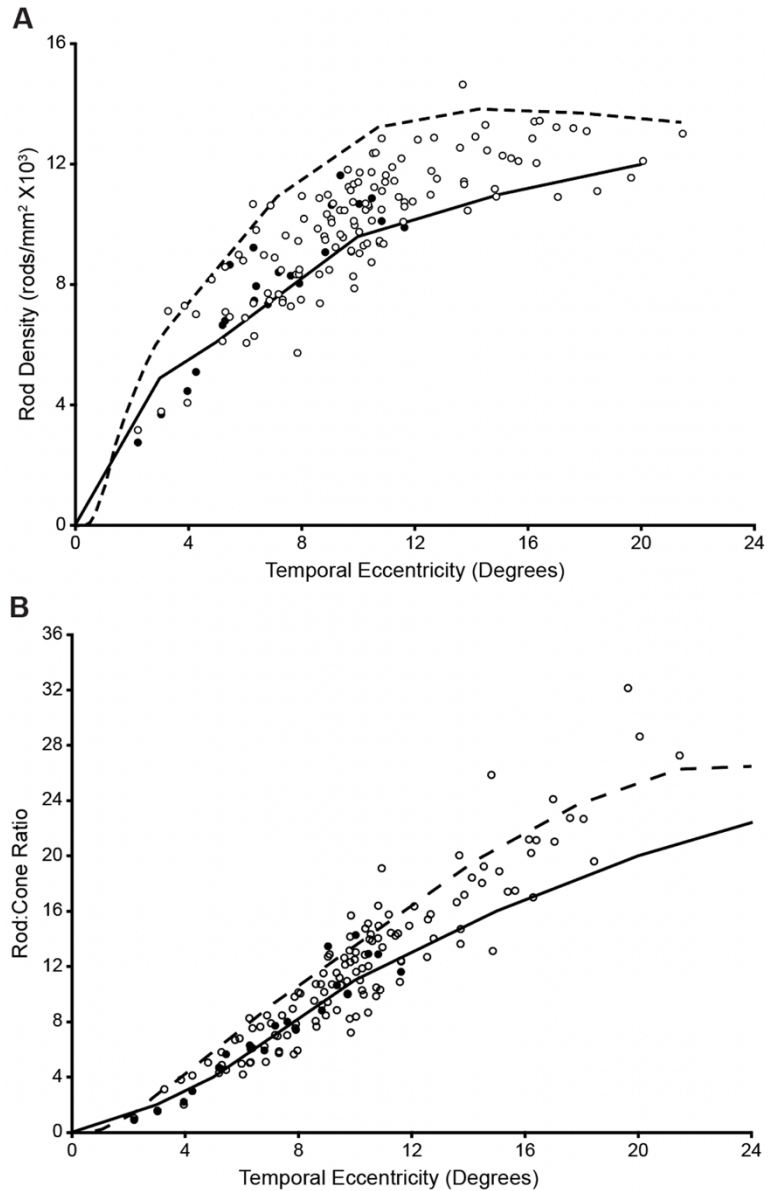
Fig. 6. Rod metrics as a function of retinal eccentricity. Previously published histological data (Curcio et al. 1990, dashed black line) and AOSLO data (Wells-Gray et al. 2016, solid black line) on rod density (A) and rod:cone ratio (B) are presented for comparison. Values derived from direct counts are represented as filled black circles while values derived from spacing are represented by open circles. See Dataset 1, Ref. [48] & Dataset 2, Ref. [49], as well as Data File 1 & Data File 2 for underlying values.

4. Discussion

Cultivating a large normative database of various rod metrics will be critical for discerning pathological changes to rod structure and topography. While rods can be visualized with advanced imaging modalities like super-resolution SLO [50], AOSLO [11], or AO-OCT [28], it can be quite challenging to consistently image rods due to their small size and reduced waveguiding relative to cones [29,30]. To date, there are limited *in vivo* normative data available on the human rod mosaic [11,23–27]. While further improvements in image resolution may be possible [27,51], we sought to explore a means of deriving estimates of rod spacing, rod density, and rod:cone ratios using existing AOSLO technology and available imagery. This method was shown to have good agreement, on average, with rod density derived from direct counts of the entire rod mosaic for a given ROI. Overall, our data agree nicely with previously published histological studies, following a similar trend as a function of retinal eccentricity [20,21,52]. On average, our rod density and rod:cone ratio estimates were 23.3% and 19.6% below that reported from histology, respectively [20]. In contrast, our estimates of rod density and rod:cone ratio were 11.3% and 15.7% higher, respectively, than previous *in vivo* measures at similar retinal locations [11]. A similar trend was observed when we evaluated our data to a study that estimated rod density from the power spectrum of an image acquired at 10° temporal to the fovea, with our rod density and rod:cone ratio estimates being 11.3% and 5.3% higher [53]. Interestingly, when compared to a separate *in vivo* study that evaluated three retinal locations, 5, 10, and 15° temporal to the fovea, our rod density estimates were 7.5% lower on average but our rod:cone ratio estimates were on average 5.4% higher [25]. Post-mortem analysis of the retinal mosaic has well-established limitations, particularly tissue shrinkage, that can alter cell spacing and density estimates by as much as 25% laterally [54] and up to 30% axially [55]. Most *in vivo* measurements available [11,22,23,25] are lower than published histological data, consistent with tissue shrinkage contributing to differences in estimates between *in vivo* and *ex vivo* studies. However, inaccuracies in the absolute scale of the *in vivo* AOSLO images could impact the accuracy of rod density estimates (both direct count and spacing derived) – it is thus important to employ methods to ensure robust determination of image scale [56].

It is important to note that metrics of the rod mosaic cannot be derived independent of information about the cone mosaic. Even when image quality is sufficient to resolve the entire rod mosaic, it is necessary to reliably disambiguate rods and cones, as some parafoveal cones can appear as small clusters of rods in confocal AOSLO images, due to propagation of higher-order waveguiding modes [57]. Here we used non-confocal AOSLO to identify cone photoreceptors [3] and effectively "mask" those regions of the corresponding confocal image, since any given point in the photoreceptor mosaic can contain either a rod or a cone (but not both). Our spacing-derived method, and similar approaches for rod metric extraction [23,53], are largely impacted by errors in cone area estimation and the assumption that the rod mosaic is regularly packed in a triangular lattice, like cones. While the rod mosaic is noncontiguous, it is presumed that rods would still have an optimized packing geometry like that observed for the cone mosaic. We believe differences in density estimated from either method presented in this study can largely be attributed to errors in estimating the total area occupied by cones within an ROI.

Rod density in this study was based on estimates of rod NND, a spacing metric insensitive to missed cells. The primary vulnerability of our method thus involves estimation of the cone area. While the semi-automated segmentation approach we used facilitated extraction of cone area estimates, defining the cone boundary is somewhat subjective in our non-confocal, split-detection images (see Fig. 1). One consideration is that the quality of split detection imagery may vary when the confocal modality is optimized for resolving the rod mosaic, as there are differences in the optimal depth of focus for rod versus cone imaging [25]. Though, even in the clearest split detection images, some cones can have nebulous edges. The subjective nature of cone segmentation may explain the significant differences observed in spacing-derived rod density

estimates across multiple graders. The four graders in this study had varying levels of experience with cone counting and segmentation but demonstrated good repeatability when analyzing the same ROI twice. For context, a one-pixel difference in cone diameter results in a 6% change in rod density. Alternative non-confocal modalities like quad-detection may enhance the contrast of cones and enable more reliable and accurate demarcation of cone boundaries (and thus more accurate estimates of cone area) [51].

An assumption of the spacing-derived method is that the rod mosaic retains a contiguous pattern, which might preclude its use on patient populations where the photoreceptor mosaic is severely disrupted, such as retinitis pigmentosa and cone-rod dystrophies [58–60]. However, in the presence of cone photoreceptor degeneration, the remaining rods can be enlarged and therefore easier to resolve [61]; making a direct counting method more practicable. Accordingly, greater success with *in vivo* imaging of the rod photoreceptor mosaic has been observed in patients with retinal disease. This has been demonstrated in female carriers of X-linked retinitis pigmentosa [62] and patients with fundus albipuntatus [63], acute macular neuroretinopathy [64], oligocone trichromacy [65], cone-rod dystrophy [61,66], blue cone monochromacy [67], achromatopsia [23,31,68], Stargardt disease [69], retinitis pigmentosa [60], and acute zonal occult outer retinopathy [23,70]. Additionally, Godara et al. demonstrated excellent resolution of the rod mosaic in patients with congenital stationary night blindness, despite normal cone density [71]. Many of these studies have extracted quantitative metrics of the rod mosaic, but often rely on normative histology data for reference. Exploring spacing-derived estimates of rod metrics in these and other disease populations are needed to test some of the regularity assumptions of the spacing-derived method, as we might expect rod and cone topography to deviate from that seen in normal retinae.

In addition to the size of retinal area sampled across eccentricity, small errors in the counting process (e.g., missing a cell) and calculation of retinal position can influence cone density estimates [7,72,73]. While there is automated software available for counting both rods and cones [74,75], the presence of both cell types within a single imaging modality can confound estimates of cell density [6]. In addition, sexually dimorphic and ethnic differences in central retinal structure have previously been reported [76] and cone packing is known to be highly variable between individuals based on axial length [11], refractive error, age [17], and eccentricity [77–79]. Therefore, a larger population including both sexes, a wide range of ages, pigmentation, refractive error, and ocular biometry should help mitigate any bias present in the current dataset. Additionally, evaluation of normal interparticipant variation in mosaic topography, as well as the interplay of the rod and cone mosaics across retinal locations should commence to establish an inclusive database.

Ultimately, improved imaging techniques [27,50] for complete resolution of the rod mosaic are crucial to gaining a full understanding of photoreceptor loss. While accurate identification of rods is necessary in order to establish a "ground truth", the method described here is beneficial in circumstances where the complete rod mosaic cannot be visualized, improving the utility of data collected using AOSLO, and in some cases enabling analysis of previously unanalyzable data. While limited to retinal areas with intact rod mosaics, this approach could be used to generate large-scale reference databases of rod density and rod:cone ratio for use in future biomarker development efforts.

5. Conclusion

While challenges remain when attempting to completely visualize the rod mosaic, this method of deriving quantitative rod metrics provides the opportunity to analyze the rod mosaic in datasets where it once was not possible. This will improve the overall value of AOSLO data by facilitating the generation of a reference database that contains a variety of rod metrics across retinal eccentricity, patient age, and patient population.

Data availability. Data underlying the results presented in this paper are available in Dataset 1 [48], Dataset 2 [49], Data File 1 [80], and Data File 2 [81].

References

1. N. Wynne, J. Carroll, and J. L. Duncan, "Promises and pitfalls of evaluating photoreceptor-based retinal disease with adaptive optics scanning light ophthalmoscopy (AOSLO)," Prog. Retinal Eye Res. **83**, 100920 (2021).
2. A. Dubra and Y. Sulai, "Reflective afocal broadband adaptive optics scanning ophthalmoscope," Biomed. Opt. Express **2**(6), 1757–1768 (2011).
3. D. Scoles, Y. N. Sulai, C. S. Langlo, G. A. Fishman, C. A. Curcio, J. Carroll, and A. Dubra, "In vivo imaging of human cone photoreceptor inner segments," Invest. Ophthalmol. Vis. Sci. **55**(7), 4244–4251 (2014).
4. R. F. Cooper, M. A. Wilk, S. Tarima, and J. Carroll, "Evaluating descriptive metrics of the human cone mosaic," Invest. Ophthalmol. Vis. Sci. **57**(7), 2992–3001 (2016).
5. K. M. Litts, R. F. Cooper, J. L. Duncan, and J. Carroll, "Photoreceptor-based biomarkers in AOSLO retinal imaging," Invest. Ophthalmol. Vis. Sci. **58**(6), BIO255 (2017).
6. J. I. W. Morgan, G. K. Vergilio, J. Hsu, A. Dubra, and R. F. Cooper, "The reliability of cone density measurements in the presence of rods," Transl. Vis. Sci. Tech. **7**(3), 21 (2018).
7. R. Garrioch, C. Langlo, A. M. Dubis, R. F. Cooper, A. Dubra, and J. Carroll, "Repeatability of in vivo parafoveal cone density and spacing measurements," Optom. Vis. Sci. **89**(5), 632–643 (2012).
8. T. Y. P. Chui, H. X. Song, and S. A. Burns, "Adaptive-optics imaging of human cone photoreceptor distribution," J. Opt. Soc. Am. A **25**(12), 3021–3029 (2008).
9. M. Bidaut Garnier, M. Flores, G. Debellemaniere, M. Puyraveau, P. Tumahai, M. Meillat, C. Schwartz, M. Montard, B. Delbosc, and M. Saleh, "Reliability of cone counts using an adaptive optics retinal camera," Clin. Exp. Ophthalmol. **42**(9), 833–840 (2014).
10. B. S. Liu, S. Tarima, A. Visotcky, A. Pechauer, R. F. Cooper, L. Landsem, M. A. Wilk, P. Godara, V. Makhijani, Y. N. Sulai, N. Syed, G. Yasumura, A. K. Garg, M. E. Pennesi, B. J. Lujan, A. Dubra, J. L. Duncan, and J. Carroll, "The reliability of parafoveal cone density measurements," Br. J. Ophthalmol. **98**(8), 1126–1131 (2014).
11. E. M. Wells-Gray, S. S. Choi, A. Bries, and N. Doble, "Variation in rod and cone density from the fovea to the mid-periphery in healthy human retinas using adaptive optics scanning laser ophthalmoscopy," Eye **30**(8), 1135–1143 (2016).
12. A. C. Bird, R. L. Phillips, and G. S. Hageman, "Geographic atrophy: a histopathological assessment," JAMA Ophthalmol. **132**(3), 338–345 (2014).
13. C. Hamel, "Retinitis pigmentosa," Orphanet J. Rare Dis. **1**(1), 40 (2006).
14. I. Ortuno-Lizaran, X. Sanchez-Saez, P. Lax, G. E. Serrano, T. G. Beach, C. H. Adler, and N. Cuenca, "Dopaminergic retinal cell loss and visual dysfunction in Parkinson Disease," Ann. Neurol. **88**(5), 893–906 (2020).
15. A. Y. Lee, C. S. Lee, M. S. Blazes, J. P. Owen, Y. Bagdasarova, Y. Wu, T. Spaide, R. T. Yanagihara, Y. Kihara, M. E. Clark, M. Kwon, C. Owsley, and C. A. Curcio, "Exploring a structural basis for delayed rod-mediated dark adaptation in age-related macular degeneration via deep learning," Transl. Vis. Sci. Tech. **9**(2), 62 (2020).
16. H. Gao and J. G. Hollyfield, "Aging of the human retina: Differential loss of neurons and retinal pigment epithelial cells," Invest. Ophthalmol. Vis. Sci. **33**, 1–17 (1992).
17. C. A. Curcio, C. L. Millican, K. A. Allen, and R. E. Kalina, "Aging of the human photoreceptor mosaic: evidence for selective vulnerability of rods in central retina," Invest. Ophthalmol. Vis. Sci. **34**, 3278–3296 (1993).
18. C. A. Curcio, C. Owsley, and G. R. Jackson, "Spare the rods, save the cones in aging and age-related maculopathy," Invest. Ophthalmol. Vis. Sci. **41**, 2015–2018 (2000).
19. T. Wang, J. Pahlberg, J. Cafaro, R. Frederiksen, A. J. Cooper, A. P. Sampath, G. D. Field, and J. Chen, "Activation of rod input in a model of retinal degeneration reverses retinal remodeling and induces formation of functional synapses and recovery of visual signaling in the adult retina," J. Neurosci. **39**(34), 6798–6810 (2019).
20. C. A. Curcio, K. R. Sloan, R. E. Kalina, and A. E. Hendrickson, "Human photoreceptor topography," J. Comp. Neurol. **292**(4), 497–523 (1990).
21. J. B. Jonas, U. Schneider, and G. O. H. Naumann, "Count and density of human retinal photoreceptors," Graefe's Arch. Clin. Exp. Ophthalmol. **230**(6), 505–510 (1992).
22. N. Doble, S. S. Choi, J. L. Codana, J. Christou, J. M. Enoch, and D. R. Williams, "In vivo imaging of the human rod photoreceptor mosaic," Opt. Lett. **36**(1), 31–33 (2011).

23. D. Merino, J. L. Duncan, P. Tiruveedhula, and A. Roorda, "Observation of cone and rod photoreceptors in normal subjects and patients using a new generation adaptive optics scanning laser ophthalmoscope," Biomed. Opt. Express **2**(8), 2189–2201 (2011).

24. J. Lu, B. Gu, X. Wang, and Y. Zhang, "High speed adaptive optics ophthalmoscopy with an anamorphic point spread function," Opt. Express **26**(11), 14356–14374 (2018).

25. A. Dubra, Y. Sulai, J. L. Norris, R. F. Cooper, A. M. Dubis, D. R. Williams, and J. Carroll, "Noninvasive imaging of the human rod photoreceptor mosaic using a confocal adaptive optics scanning ophthalmoscope," Biomed. Opt. Express **2**(7), 1864–1876 (2011).

26. R. F. Cooper, A. M. Dubis, A. Pavaskar, J. Rha, A. Dubra, and J. Carroll, "Spatial and temporal variation of rod photoreceptor reflectance in the human retina," Biomed. Opt. Express **2**(9), 2577–2589 (2011).

27. R. Lu, N. Aguilera, T. Liu, J. Liu, J. P. Giannini, J. Li, A. J. Bower, A. Dubra, and J. Tam, "In-vivo sub-diffraction adaptive optics imaging of photoreceptors in the human eye with annular pupil illumination and sub-Airy detection," Optica **8**(3), 333–343 (2021).

28. E. M. Wells-Gray, S. S. Choi, R. J. Zawadzki, S. C. Finn, C. Greiner, J. S. Werner, and N. Doble, "Volumetric imaging of rod and cone photoreceptor structure with a combined adaptive optics-optical coherence tomography-scanning laser ophthalmoscope," J. Biomed. Opt. **23**(03), 1–15 (2018).

29. M. Alpern, C. C. Ching, and K. Kitahara, "The directional sensitivity of retinal rods," J. Physiol. **343**(1), 577–592 (1983).

30. J. A. van Loo and J. M. Enoch, "The scoptopic Stiles-Crawford effect," Vision Res. **15**(8-9), 1005–1009 (1975).

31. J. Carroll, S. S. Choi, and D. R. Williams, "In vivo imaging of the photoreceptor mosaic of a rod monochromat," Vision Res. **48**(26), 2564–2568 (2008).

32. J. A. Cava, M. T. Allphin, R. R. Mastey, M. Gaffney, R. E. Linderman, R. F. Cooper, and J. Carroll, "Assessing interocular symmetry of the foveal cone mosaic," Invest. Ophthalmol. Visual Sci. **61**(14), 23 (2020).

33. S. Steven, Y. N. Sulai, S. K. Cheong, J. Bentley, and A. Dubra, "Long eye relief fundus camera and fixation target with partial correction of ocular longitudinal chromatic aberration," Biomed. Opt. Express **9**(12), 6017–6037 (2018).

34. A. Dubra and Z. Harvey, "Registration of 2D images from fast scanning ophthalmic instruments," in *Biomedical Image Registration*, B. Fischer, B. Dawant, and C. Lorenz, eds. (Springer-Verlag, 2010), pp. 60–71.

35. A. E. Salmon, R. F. Cooper, C. S. Langlo, A. Baghaie, A. Dubra, and J. Carroll, "An automated reference frame selection (ARFS) algorithm for cone imaging with adaptive optics scanning light ophthalmoscopy," Trans. Vis. Sci. Tech. **6**(2), 9 (2017).

36. A. E. Salmon, R. F. Cooper, and J. Carroll, "Effect of intraframe motion correction on residual distortion in AOSLO images," *Invest. Ophthalmol. Vis. Sci.* 60, E-Abstract: 4606 (2019).

37. M. Chen, R. F. Cooper, J. C. Gee, D. H. Brainard, and J. I. W. Morgan, "Automatic longitudinal montaging of adaptive optics retinal images using constellation matching," Biomed. Opt. Express **10**(12), 6476–6496 (2019).

38. K. M. Litts, M. Georgiou, C. S. Langlo, E. J. Patterson, R. R. Mastey, A. Kalitzeos, R. E. Linderman, B. L. Lam, G. A. Fishman, M. E. Pennesi, C. N. Kay, W. W. Hauswirth, M. Michaelides, and J. Carroll, "Interocular symmetry of foveal cone topography in congenital achromatopsia," Curr. Eye Res. **45**(10), 1257–1264 (2020).

39. H. Emsley, *Visual Optics* (Butterworth & Co, 1953).

40. C. A. Schneider, W. S. Rasband, and K. W. Eliceiri, "NIH Image to ImageJ: 25 years of image analysis," Nat. Methods **9**(7), 671–675 (2012).

41. J. Liu, H. Jung, A. Dubra, and J. Tam, "Cone photoreceptor cell segmentation and diameter measurement on adaptive optics images using circularly constrained active contour model," Invest. Ophthalmol. Visual Sci. **59**(11), 4639–4652 (2018).

42. N. J. Coletta and D. R. Williams, "Psychophysical estimate of extrafoveal cone spacing," J. Opt. Soc. Am. A **4**(8), 1503–1513 (1987).

43. D. R. Williams and N. J. Coletta, "Cone spacing and the visual resolution limit," J. Opt. Soc. Am. A **4**(8), 1514–1523 (1987).

44. J. M. Bland and D. G. Altman, "Statistical methods for assessing agreement between two methods of clinical measurement," Lancet **327**(8476), 307–310 (1986).

45. J. M. Bland and D. G. Altman, "Measuring agreement in method comparison studies," Stat. Methods Med. Res. **8**(2), 135–160 (1999).

46. J. M. Bland and D. G. Altman, "Applying the right statistics: analyses of measurement studies," Ultrasound Obstet. Gynecol. **22**(1), 85–93 (2003).

47. J. M. Bland and D. G. Altman, "Statistics notes: Measurement error proportional to the mean," Br. Med. J. **313**(7049), 106 (1996).

48. H. Heitkotter, E. J. Patterson, E. N. Woertz, J. A. Cava, M. Gaffney, I. Adhan, J. Tam, R. F. Cooper, and J. Carroll, "Dataset 1: Direct count ROIs," figshare (2022) https://doi.org/10.6084/m9.figshare.20477163

49. H. Heitkotter, E. J. Patterson, E. N. Woertz, J. A. Cava, M. Gaffney, I. Adhan, J. Tam, R. F. Cooper, and J. Carroll, "Dataset 2: Spacing-derived ROIs," figshare (2022) https://doi.org/10.6084/m9.figshare.20477169

50. Y. Lu, T. Son, T. H. Kim, D. Le, and X. Yao, "Virtually structured detection enables super-resolution ophthalmoscopy of rod and cone photoreceptors in human retina," Quant. Imaging Med. Surg. **11**(3), 1060–1069 (2020).

51. N. Sredar, O. E. Fagbemi, and A. Dubra, "Sub-airy confocal adaptive optics scanning ophthalmoscopy," Trans. Vis. Sci. Tech. **7**(2), 17 (2018).

52. P. K. Ahnelt, "The photoreceptor mosaic," Eye **12**(3), 531–540 (1998).

53. R. F. Cooper, C. S. Langlo, A. Dubra, and J. Carroll, "Automatic detection of modal spacing (Yellott's ring) in adaptive optics scanning light ophthalmoscope images," Ophthalmic Physiol. Opt. **33**, 540–549 (2013).

54. C. J. Abbott, N. A. McBrien, G. U. and M, and J. Pianta, "Relationship of the optical coherence tomography signal to underlying retinal histology in the tree shrew (*Tupaia belangeri*)," Invest. Ophthalmol. Visual Sci. **50**(1), 414–423 (2009).

55. C. A. Curcio, J. D. Messinger, K. R. Sloan, A. Mitra, G. McGwin, and R. F. Spaide, "Human chorioretinal layer thicknesses measured in macula-wide, high-resolution histologic sections," Invest. Ophthalmol. Visual Sci. **52**(7), 3943–3954 (2011).

56. X. Huang, T. Anderson, and A. Dubra, "Retinal magnification factors at the fixation locus derived from schematic eyes with four individualized surfaces," Biomed. Opt. Express **13**(7), 3786–3808 (2022).

57. J. M. Enoch, J. Tobey, and F., "Waveguide properties of retinal receptors: Techniques and observations," in *Vertebrate Photoreceptor Optics*, J. M. Enoch, J. Tobey, and F. l., eds. (Springer-Verlag, 1981), pp. 169–218.

58. J. Carroll, R. C. Baraas, M. Wagner-Schuman, J. Rha, C. A. Siebe, C. Sloan, D. M. Tait, S. Thompson, J. I. Morgan, J. Neitz, D. R. Williams, D. H. Foster, and M. Neitz, "Cone photoreceptor mosaic disruption associated with Cys203Arg mutation in the M-cone opsin," Proc. Natl. Acad. Sci. U. S. A. **106**(49), 20948–20953 (2009).

59. J. L. Duncan, Y. Zhang, J. Gandhi, C. Nakanishi, M. Othman, K. E. Branham, A. Swaroop, and A. Roorda, "High-resolution imaging with adaptive optics in patients with inherited retinal degeneration," Invest. Ophthalmol. Visual Sci. **48**(7), 3283–3291 (2007).

60. L. W. Sun, R. D. Johnson, C. S. Langlo, R. F. Cooper, M. M. Razeen, M. C. Russillo, A. Dubra, T. B. Connor Jr., D. Han, M. E. Pennesi, C. N. Kay, D. V. Weinberg, K. E. Stepien, and J. Carroll, "Assessing photoreceptor structure in retinitis pigmentosa and Usher syndrome," Invest. Ophthalmol. Visual Sci. **57**(6), 2428–2442 (2016).

61. H. Song, E. A. Rossi, E. Stone, L. Latchney, D. Williams, A. Dubra, and M. Chung, "Phenotypic diversity in autosomal-dominant cone-rod dystrophy elucidated by adaptive optics retinal imaging," Br. J. Ophthalmol. **102**(1), 136–141 (2018).

62. A. Kalitzeos, R. Samra, M. Kasilian, J. L. Tee, M. Strampe, C. Langlo, A. R. Webster, A. Dubra, J. Carroll, and M. Michaelides, "Cellular imaging of the tapetal-like reflex in carriers of *RPGR*-associated retinopathy," Retina **39**(3), 570–580 (2019).

63. E. K. Sobol, A. Deobhakta, C. S. Wilkins, J. H. Francis, T. Y. P. Chui, A. Dubra, D. B. Zhuo, M. V. Castanos, G. M. C. Lema, R. B. Rosen, and J. V. Migacz, "Fundus albipunctatus photoreceptor microstructure revealed using adaptive optics scanning light ophthalmoscopy," Am. J. Ophthalmol. Case Rep. **22**, 101090 (2021).

64. S. O. Hansen, R. F. Cooper, A. Dubra, J. Carroll, and D. V. Weinberg, "Selective cone photoreceptor injury in acute macular neuroretinopathy," Retina **33**(8), 1650–1658 (2013).

65. J. Li, T. Liu, O. J. Flynn, A. Turriff, Z. Liu, E. Ullah, J. Liu, A. Dubra, M. A. Johnson, B. P. Brooks, R. B. Hufnagel, D. X. Hammer, L. A. Huryn, B. G. Jeffrey, and J. Tam, "Persistent dark cones in oligocone trichromacy revealed by multimodal adaptive optics ophthalmoscopy," Front. Aging Neurosci. **13**, 629214 (2021).

66. D. Scoles, J. A. Flatter, R. F. Cooper, C. S. Langlo, S. Robison, M. Neitz, D. V. Weinberg, M. E. Pennesi, D. P. Han, A. Dubra, and J. Carroll, "Assessing photoreceptor structure associated with ellipsoid zone disruptions visualized with optical coherence tomography," Retina **36**(1), 91–103 (2016).

67. J. Carroll, A. Dubra, J. C. Gardner, L. Mizrahi-Meissonnier, R. F. Cooper, A. M. Dubis, R. Nordgren, M. Genead, T. B. Connor Jr, K. E. Stepien, D. Sharon, D. M. Hunt, E. Banin, A. J. Hardcastle, A. T. Moore, D. R. Williams, G. Fishman, J. Neitz, M. Neitz, and M. Michaelides, "The effect of cone opsin mutations on retinal structure and the integrity of the photoreceptor mosaic," Invest. Ophthalmol. Visual Sci. **53**(13), 8006–8015 (2012).

68. C. S. Langlo, E. J. Patterson, B. P. Higgins, P. Summerfelt, M. M. Razeen, L. R. Erker, M. Parker, F. T. Collison, G. A. Fishman, C. N. Kay, J. Zhang, R. G. Weleber, P. Yang, D. J. Wilson, M. E. Pennesi, B. L. Lam, J. Chiang, J. D. Chulay, A. Dubra, W. W. Hauswirth, and J. Carroll, and ACHM-001 Study Group, "Residual foveal cone structure in CNGB3-associated achromatopsia," Invest. Ophthalmol. Visual Sci. **57**(10), 3984–3995 (2016).

69. H. Song, E. A. Rossi, L. Latchney, A. Bessette, E. Stone, J. J. Hunter, D. R. Williams, and M. Chung, "Cone and rod loss in Stargardt disease revealed by adaptive optics scanning light ophthalmoscopy," JAMA Ophthalmol. **133**(10), 1198–1203 (2015).

70. M. Mkrtchyan, B. J. Lujan, D. Merino, C. E. Thirkill, A. Roorda, and J. L. Duncan, "Outer retinal structure in patients with acute zonal occult outer retinopathy," Am. J. Ophthalmol. **153**(4), 757–768.e1 (2012).

71. P. Godara, R. F. Cooper, P. I. Sergouniotis, M. A. Diederichs, M. R. Streb, M. A. Genead, J. J. McAnany, A. R. Webster, A. T. Moore, A. M. Dubis, M. Neitz, A. Dubra, E. M. Stone, G. A. Fishman, D. P. Han, M. Michaelides, and J. Carroll, "Assessing retinal structure in complete congenital stationary night blindness and Oguchi disease," Am. J. Ophthalmol. **154**(6), 987–1001.e1 (2012).

72. M. Lombardo, S. Serrao, P. Ducoli, and G. Lombardo, "Eccentricity dependent changes of density, spacing and packing arrangement of parafoveal cones," Ophthalmic Physiol. Opt. **33**(4), 516–526 (2013).

73. M. Lombardo, S. Serrao, P. Ducoli, and G. Lombardo, "Influence of sampling window size and orientation on parafoveal cone packing density," Biomed. Opt. Express **4**(8), 1318–1331 (2013).

74. D. Cunefare, A. L. Huckenpahler, E. J. Patterson, A. Dubra, J. Carroll, and S. Farsiu, "RAC-CNN: Multimodal deep learning based automatic detection and classification of rod and cone photoreceptors in adaptive optics scanning light ophthalmoscope images," Biomed. Opt. Express **10**(8), 3815–3832 (2019).

75. S. J. Chiu, Y. Lokhnygina, A. M. Dubis, A. Dubra, J. Carroll, J. A. Izatt, and S. Farsiu, "Automatic cone photoreceptor segmentation using graph theory and dynamic programming," Biomed. Opt. Express **4**(6), 924–937 (2013).

76. M. Wagner-Schuman, A. M. Dubis, R. N. Nordgren, Y. Lei, D. Odell, H. Chiao, E. Weh, W. Fischer, Y. Sulai, A. Dubra, and J. Carroll, "Race- and sex-related differences in retinal thickness and foveal pit morphology," Invest. Ophthalmol. Visual Sci. **52**(1), 625–634 (2011).

77. T. Y. Chui, H. Song, and S. A. Burns, "Individual variations in human cone photoreceptor packing density: Variations with refractive error," Invest. Ophthalmol. Visual Sci. **49**(10), 4679–4687 (2008).

78. H. Song, T. Y. Chui, Z. Zhong, A. E. Elsner, and S. A. Burns, "Variation of cone photoreceptor packing density with retinal eccentricity and age," Invest. Ophthalmol. Visual Sci. **52**(10), 7376–7384 (2011).

79. Y. Wang, N. Bensaid, P. Tiruveedhula, J. Ma, S. Ravikumar, and A. Roorda, "Human foveal cone photoreceptor topography and its dependence on eye length," eLife **8**, e47148 (2019).

80. H. Heitkotter, E. J. Patterson, E. N. Woertz, J. A. Cava, M. Gaffney, I. Adhan, J. Tam, R. F. Cooper, and J. Carroll, "Data file 1: Direct Count Rod Metrics," figshare (2022) https://doi.org/10.6084/m9.figshare.21568869

81. H. Heitkotter, E. J. Patterson, E. N. Woertz, J. A. Cava, M. Gaffney, I. Adhan, J. Tam, R. F. Cooper, and J. Carroll, "Data file 2: Spacing-derived Rod Metrics," figshare (2022) https://doi.org/10.6084/m9.figshare.21568872